nature catalysis

Article

https://doi.org/10.1038/s41929-025-01306-9

Enantioselective C–H annulations enabled by either nickel- or cobalt-electrocatalysed C–H activation for catalyst-controlled chemodivergence

Received: 21 December 2023

Accepted: 10 February 2025

Published online: 7 March 2025

Check for updates

Tristan von Münchow[1,2], Neeraj Kumar Pandit[1,2], Suman Dana[1], Philipp Boos[1], Sven Erik Peters[1], Josselin Boucat[1], Yi-Ru Liu[1], Alexej Scheremetjew[1] & Lutz Ackermann[1]

Enantioselective electrocatalysis shows unique potential for the sustainable assembly of enantiomerically enriched molecules. This approach allows electro-oxidative C–H activation to be performed paired to the hydrogen evolution reaction. Recent progress has featured scarce transition metals with limited availability. Here we reveal that the earth-abundant 3*d* transition metals nickel and cobalt exhibit distinctive performance for enantioselective electrocatalysis with chemodivergent reactivity patterns. Enantioselective desymmetrizations of strained bicyclic alkenes were achieved through C–H annulations. A data-driven optimization of chiral *N*,*O*-bidentate salicyloxazoline-type ligands was crucial for enhancing enantioselectivity in nickel electrocatalysis. Notably, in the transition state of the enantio-determining step, secondary weak attractive π–π and CH–π interactions were identified, reflecting the informed adaptations in the ligand design. Detailed mechanistic investigations by experimental and computational studies revealed for the nickel electrocatalysis a C–N bond-forming reductive elimination from nickel(III) and for the cobalt electrocatalysis a C–C bond-forming nucleophilic addition from cobalt(III) as the product-determining steps.

In recent years, enantioselective electrochemical transition-metal catalysis has been recognized as a resource-economic tool for the synthesis of chiral organic architectures[1–7]. In this innovative strategy, catalytic transformations are enabled by the electrochemical redox manipulation of transition-metal catalysts, avoiding the use of sacrificial redox agents. In particular, in electro-oxidative catalysis, the redox equivalents are provided by the formation of molecular hydrogen through the paired cathodic hydrogen evolution reaction (HER)[6–9], offering a transformative platform to address the growing global demand for efficient and clean energy solutions[10–13].

Despite these beneficial features, so far, enantioselective electro-oxidative C–H activation reactions have been severely limited to transition metals with high risk of future supply shortages[14,15], such as the precious 4*d* transition metals palladium[16–18] and rhodium[19–21], whereas narrow diversity in terms of reaction pathways has been developed for cobalt[22–28]. Hence, the further exploration of transition metals with high natural abundance[29] is of major interest in this domain.

[1]Institut für Organische und Biomolekulare Chemie, Wöhler Research Institute for Sustainable Chemistry, Georg-August-Universität Göttingen, Göttingen, Germany. [2]These authors contributed equally: Tristan von Münchow, Neeraj Kumar Pandit. e-mail: lutz.ackermann@chemie.uni-goettingen.de

https://doi.org/10.1038/s41929-025-01306-9

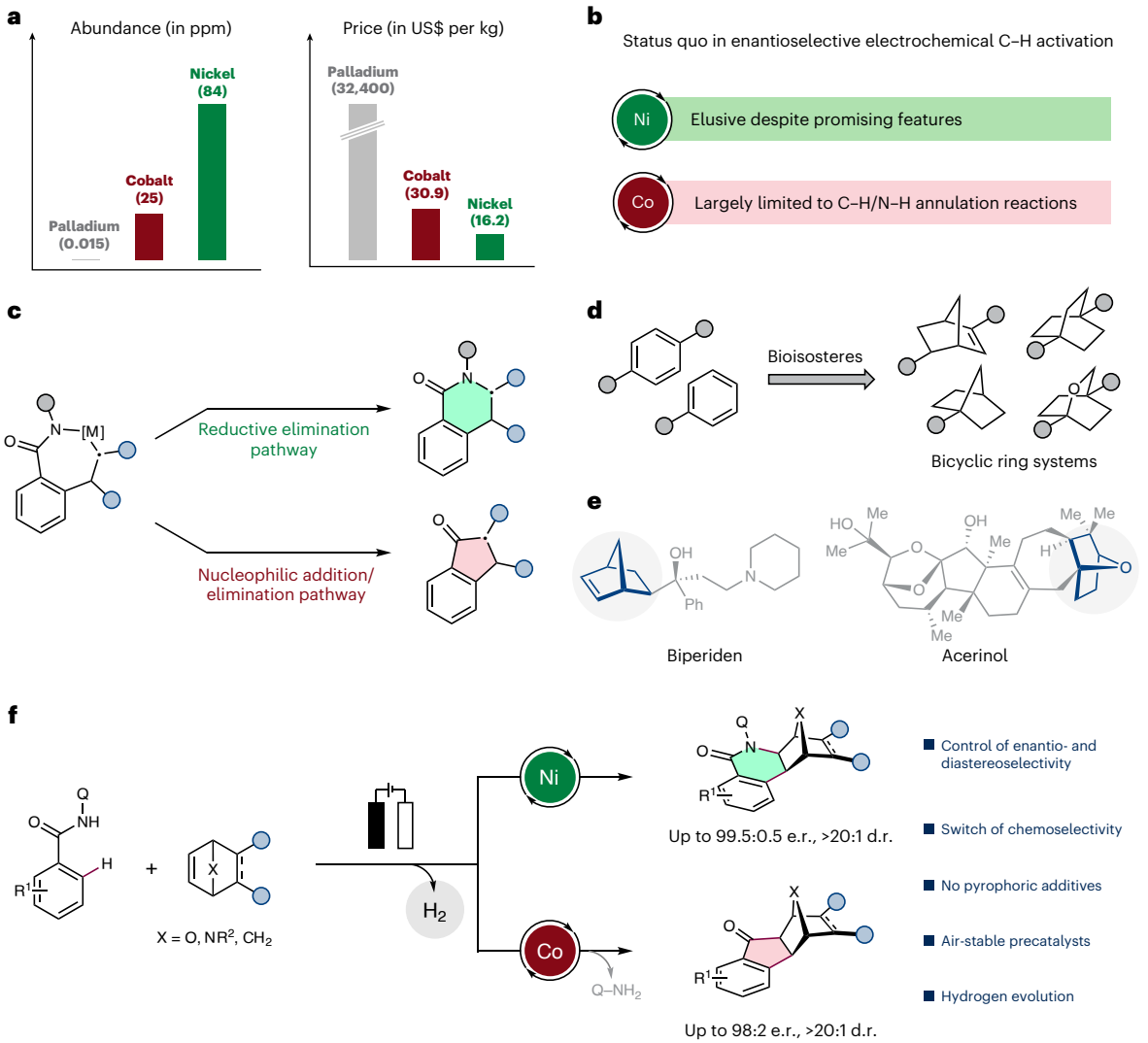

Fig. 1 | Enantioselective electrochemical C–H activation for full selectivity control. a, Sustainability aspects of selected transition metals in comparison. **b**, Motivation for the development of enantioselective electrochemical C–H activation by 3*d* transition-metal catalysis. **c**, Divergent reaction pathways in alkene C–H annulations. **d**, Bicyclic bridged ring systems as bioisosteres for benzene derivatives. **e**, Selected chiral biologically active compounds containing bicyclo[2.2.1]heptane skeletons. **f**, Chemodivergent desymmetrizations enabled by electrocatalytic C–H activation (this work). e.r., enantiomeric ratio; d.r., diastereomeric ratio.

Besides cobalt, the cost-effective[30] and less toxic[31,32] base metal nickel is particularly attractive as a catalyst, which, owing to its flexibility in adopting various oxidation states, displays unique reactivity patterns for homogeneous catalysis[33–35] (Fig. 1a).

The versatility of nickel catalysis for enantioselective synthesis has been explored and studied in systems that operate via mechanisms such as ligand-to-ligand hydrogen transfer[36,37] and radical processes[38–40], as well as in reductive homo- and cross-coupling reactions[41–45]. However, the direct activation of inert C–H bonds under nickel catalysis typically requires harsh reaction conditions, rendering the development of enantioselective methodologies very challenging[46,47]. The enantioselective catalytic C–H activations described are limited to highly sensitive, low-valent nickel(0) precatalysts using chiral N-heterocyclic carbene (NHC)[48] or heteroatom-substituted secondary phosphine oxide (HASPO)[49,50] (pre)ligands and commonly rely on pyrophoric organoaluminium reagents[51,52]. Thus, enabling oxidative nickel-catalysed C–H activation with chiral ligands for effective enantio-induction within an electro-oxidative high-valent nickel regime is a formidable challenge (Fig. 1b).

Furthermore, enantioselective electrochemical C–H activation enabled by cobalt catalysis, beyond the generally observed C–H/N–H annulation[22–25,27,28], would represent a major advancement to expand the diversity of molecular motifs accessible through electro-oxidative 3*d* transition-metal catalysis (Fig. 1c).

Nickel and cobalt can exhibit similar chemical behaviour[53,54], having comparable atomic radii[55]. However, the electronegativities[56] and electronic configurations for a specific oxidation state in their coordination complexes differ, resulting in distinct properties and reactivities[57–59]. Yet, the implication of these differentiating features in enantioselective electrochemical C–H activation has not been elucidated.

Here, we report on enantioselective electrocatalytic desymmetrizations of strained bicyclic alkenes through nickel- and cobalt-catalysed C–H activation giving access to substituted chiral sp^3-rich ring systems—skeletons encountered in various biologically active compounds and of medicinal relevance (Fig. 1d,e)[60–64]. Intriguingly, the devised enantioselective C–H activations reveal a chemodivergence (Fig. 1f). While the nickel electrocatalysis is selective for

carboamination via reductive elimination, the cobalt electrocatalysis furnishes the carboacylation product through a nucleophilic addition/elimination pathway.

Results

Development of the enantioselective nickel electrocatalysis

We initiated our studies by evaluating nickel(II) acetate as the catalyst for the electro-oxidative C–H activation of benzamide **1** with the bicyclic alkene **2** (refs. 65–67). To our delight, by exploiting chiral salicyloxazoline ligands[68], the carboamination product **3** was formed under galvanostatic conditions with promising enantiocontrol (Fig. 2a). However, by pure empirical reaction optimization, it was challenging to identify a ligand that would enhance the catalysis selectivity and performance. Thus, a data-driven approach[69,70] was pursued to assist in the ligand development. Following the workflow described in Fig. 2b with ligand screening data, we commenced by optimizing the free ligand structures at the TPSS-D3(BJ)/def2-SVP level of theory, followed by single-point calculations at the PW6B95-D3(BJ)/def2-TZVPP+SMD(1,4-dioxane) level of theory to acquire density functional theory (DFT)-derived descriptors (for further details, see 'Development of nickel catalysis' in the Supplementary Methods). A wide range of descriptors[71] were explored to describe the variations in the ligand structures as well as their properties. For electronic features, frontier molecular orbital energies, natural bond orbital (NBO) charges and net dipole moments (μ_{net}) were derived from single-point DFT calculations. To assess the steric and geometric properties, sterimol parameters[72] B_{min}, B_{max} and L were considered, where B_{min} and B_{max} represent the minimum and maximum perpendicular widths of the substituent, respectively, while L corresponds to its axial length along the measured bond axis, together with dihedral angles. In light of recent studies[73,74] demonstrating the use of vibrational features for integrated effects of steric behaviour and charge layout, vibrational modes of the ligand were also used.

Based on the feature importance analysis using a tree-based regression model (random forest regressor) on the obtained ligand screening data, steric parameter of C11 substituent (R1_L), asymmetric stretching mode 1 from phenyl ring (asym1_v) and NBO charge at C10 carbon (NBO_C10) emerged as the top three crucial ligand features, notably affecting the enantioselectivity. In model screening, the gradient boosting regression (GBR) model proved to be the best model with the least test and validation mean absolute error (MAE_{test} 0.32 kcal mol^{-1} and $MAE_{validation}$ 0.19 kcal mol^{-1}) on the training and validation dataset. Later, the permutation analysis on the trained GBR model likewise showed similar feature importance with NBO_C10 as the most crucial feature after the R1_L. Based on the most relevant features, five ligands with variable substitution patterns were thereby newly designed, which were expected to be more prominent. The constructed model was used to predict the enantioselectivity ($\Delta\Delta G_{pred}$) for the five devised ligands, followed by prediction evaluation with experimentally obtained $\Delta\Delta G_{exp}$. In agreement with the GBR model, ligand **L7** was identified as the best-performing ligand within the group of newly designed ligands and overall dataset. Thus, with the help of feature analysis, the considered substitutional modifications to the ligand backbone resulted in a newly designed ligand variant **L7** exhibiting effective enantio-induction for the challenging stereo-control in electro-oxidative nickel-catalysed C–H activation (Fig. 2b; for further details, see 'Development of nickel catalysis' in the Supplementary Methods). Finally, all the studied ligands (initially screened and newly designed) were projected in the top three feature space. The feature space was clearly able to separate the new ligands from the initially screened ones, indicating the contrasting feature values.

To rationalize the high efficiency of the devised ligand **L7** in controlling the stereoselectivity in the nickel electrocatalysis, a non-covalent interaction (NCI)[75,76] analysis of the transition state (**TS1**[2]) involved in the migratory insertion was carried out (Fig. 2c; for the energy profile, see 'Computational studies for nickel catalysis' in the Supplementary Methods). Here, a substantial secondary attractive π–π interaction between the arene at the oxazoline (C11) from the ligand **L7** and the 8-quinolinyl of the benzamide was identified, along with a weak attractive CH–π interaction between the methyl at oxazoline (C10) and benzene plane of the benzamide. Furthermore, the role of the NCIs in stabilizing the **TS1** was thoroughly evaluated with three additional ligands (**L3**, **L5** and **L6**). The substitution patterns later presented were differentiated with the **L7**, allowing to single out the relevant NCIs. The comparison of energy barriers for the enantio-determining step (**TS1**) for both enantiomers revealed that **L7** requires a lower energy barrier ($\Delta G^{\ddagger}$ = 22.8 kcal mol^{-1}) than the other considered ligands. We observed that the dispersive π–π interactions present a more prominent stabilizing effect than the CH–π interactions, as the absence of solely CH–π interactions led to an increase of energy barrier for the **TS1** by 0.6 kcal mol^{-1} (**L6**), whereas the absence of both increased the energy barrier to 2.9 kcal mol^{-1} (**L5**). Moreover, the removal of *tert*-butyl groups (**L3**) led to a considerable decrease in enantioselectivity (Gibbs free energy difference between the transition states, $\Delta\Delta G^{\ddagger}$ = −2.4 kcal mol^{-1}). These findings highlight the ligand effect in the catalyst stabilization, facilitating the migratory insertion of the alkene. Interestingly, these two ligand site feature roles (R1_L, and NBO_C10) were also indicated by the early feature analysis and post-model development. In addition, the NCI plot unveiled a strong attractive polar interaction between oxygen of the 7-oxabenzonorbornadiene and carbonyl carbon centre from the benzamide, aligning with the experimentally observed excellent diastereoselectivity. With a suitable ligand for superior enantio-induction being identified by data science, we next improved the efficacy of the catalysis further (Fig. 3a). Hence, we monitored the reaction progress during electrocatalysis and found that, already in the initial stage, the formation of product **3** proceeded only gradually, pointing at an inefficient anodic electron transfer. For this purpose, we probed ferrocene (Cp_2Fe) as a redox mediator, which led to a considerable increase in the efficiency while maintaining the excellent control of enantioselectivity (Fig. 3a, entries 1 and 2, and Fig. 3b). Under the improved reaction conditions, we reevaluated ligand **L6**. Here, we could experimentally support the importance of the methyl groups on the oxazoline (C10) for an effective enantiocontrol as **L6** exhibited reduced enantioselectivity compared with **L7**. The achiral ligands **L8** and **L9** led to racemic product **3** with high levels of diastereoselectivity of >20:1 (Fig. 3a, entries 3–6, and Fig. 3c).

Versatility of the enantioselective nickel electrocatalysis

With the optimized conditions, the versatility of the nickel electrocatalysis was examined (Fig. 3d). The strategy enabled the synthesis of a broad range of chiral bridged dihydroisoquinolinones in high enantiomeric excess (**3** and **5**–**38**) thereby tolerating various functional groups. The strategy showed high tolerance to oxidation-sensitive thioether groups (**7** and **18**) and electrophilic carbonyl motifs (**8**–**10**, **20** and **26**). Besides fluoro- (**16**), bromo- (**6**) and iodo- (**15**) substituents, benzamides bearing an acetamido motif (**21**) as well as benzamides featuring sterically demanding 3,5-disubstitution (**23**–**26**) were found to be compatible. In addition, the electrocatalytic C–H activation on thiophene enabled the enantioselective synthesis of the desired carboamination products (**22** and **36**). Moreover, the devised electrocatalysis was not only limited to 7-oxabenzonorbornadienes; with norbornadiene (**29**), norbornene (**30**) and 7-azabenzonorbornadienes (**31** and **32**) the desired product formation with satisfying enantiocontrol was also achieved.

Mechanistic elucidation of the nickel manifold

We were then interested in investigating the mechanism of enantioselective high-valent nickel-catalysed C–H activation in more detail (Figs. 4 and 5). First, a kinetic isotope effect (KIE) study of the devised nickel electrocatalysis was conducted, which yielded k_H/k_D = 1.1 (where k_H and k_D are the rate constants for the electrocatalysis involving **1** or

https://doi.org/10.1038/s41929-025-01306-9

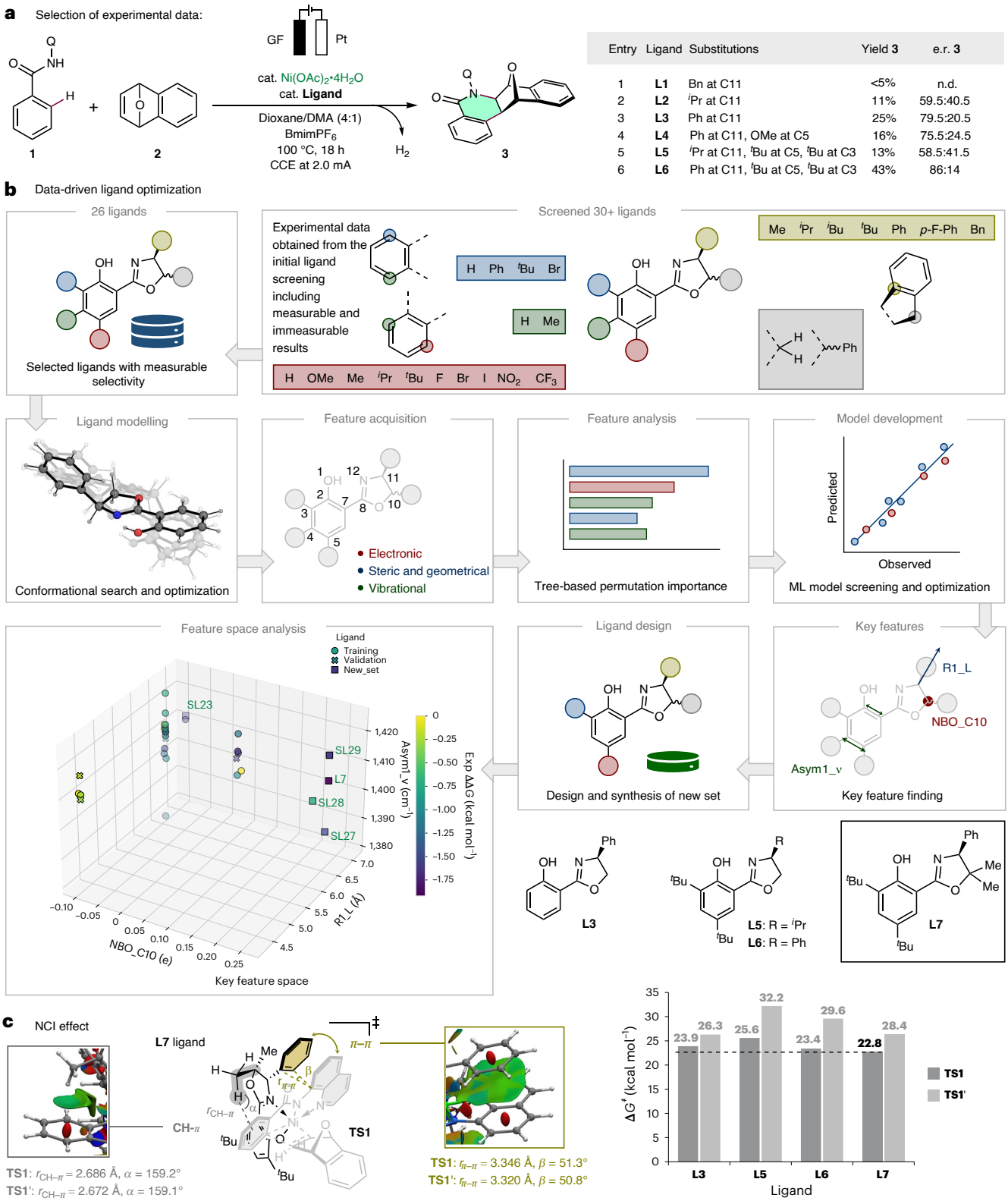

Fig. 2 | Data-driven optimization of the chiral ligand. a, Initial experimental ligand screening. Reaction conditions: **1** (0.2 mmol), **2** (0.3 mmol), $Ni(OAc)_2{\cdot}4H_2O$ (0.04 mmol), ligand (0.06 mmol), $BmimPF_6$ (0.05 M), 1,4-dioxane/DMA (4:1, v/v, 5 ml). Undivided cell. GF, graphite felt anode; Pt, platinum plate cathode. Stirring rate, 600 rpm. Constant current electrolysis (CCE) at 2.0 mA. 100 °C, 18 h reaction time. Q, 8-quinolinyl; Bmim, 1-butyl-3-methylimidazolium; cat., catalytic; n.d., not detected. **b**, The general workflow for data-driven ligand optimization with the final top three feature space. ML, machine learning; Exp, experimental. **c**, Respective visualizations of the NCIs ($\pi-\pi$ and CH$-\pi$) in **TS1** with **L7** are made with the NCIPLOT program. Selected distances and angles are shown for **TS1** and **TS1′**. Red represents strong repulsive interactions in the plotted surfaces, whereas green and blue represent weak and strong attractive interactions, respectively. Energies are with reference to the **Int0L7** in the ligand comparison plot. $\Delta\Delta G$, Gibbs free energy difference between the major and minor product isomers; $\Delta G^{\ddagger}$, Gibbs free energy difference between reactant (**Int0L7**) and transition state.

https://doi.org/10.1038/s41929-025-01306-9

a

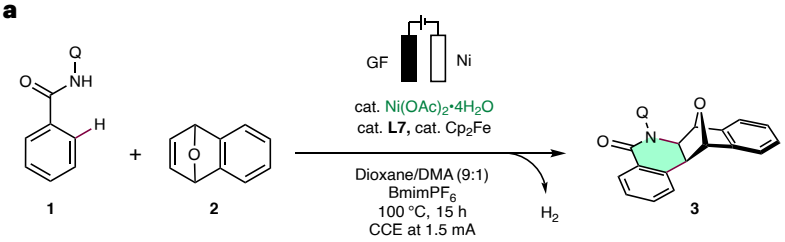

Entry	Deviation from the standard conditions	Yield **3**	e.r. **3**	d.r. **3**
1	–	70%	95:5	>20:1
2	No Cp_2Fe	25%	93:7	>20:1
3	**L6** instead of **L7**	48%	90:10	>20:1
4	**L8** instead of **L7**	45%	50:50	>20:1
5	**L9** instead of **L7**	46%	50:50	>20:1
6	No chiral ligand	57%	50:50	>20:1
7	$Co(OAc)_2·4H_2O$ instead of $Ni(OAc)_2·4H_2O$	<5%	–	–

b

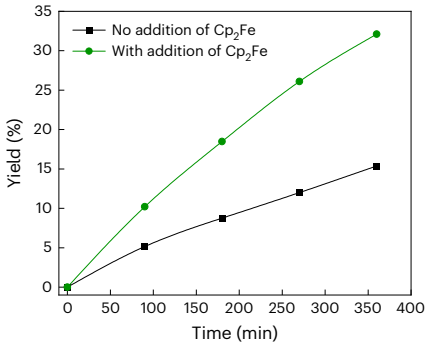

c

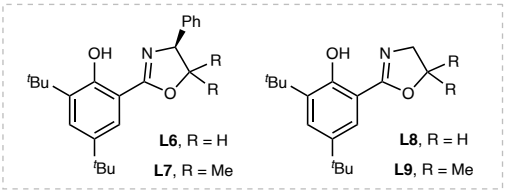

d

3, R = H, 70%, 95:5 e.r.
5, R = Me, 56%, 92:8 e.r.
6, R = Br, 52%, 92.5:7.5 e.r.
7, R = SMe, 60%, 91.5:8.5 e.r.
8, R = OAc, 58%, 96:4 e.r.
9, R = CO_2Me, 38%, 94.5:5.5 e.r., CCDC 2278175
10, R = (CO)Me, 42%, 94:6 e.r.
11, R = OPh, 64%, 84.5:15.5 e.r.
12, R = OTBDMS, 68%, 94:6 e.r.

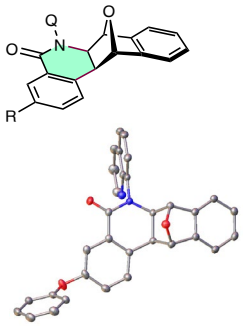

11, CCDC 2278176

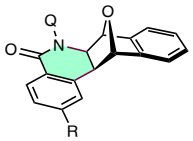

13, R = Et, 65%, 95:5 e.r.
14, R = ^{t}Bu, 57%, 96.5:3.5 e.r.
15, R = I, 55%, 91:9 e.r.
16, R = F, 48%, 93.5:6.5 e.r.
17, R = OMe, 42%, 94.5:5.5 e.r.
18, R = SMe, 79%, 96:4 e.r.
19, R = OPiv, 71%, 92:8 e.r.
20, R = CO_2Me, 51%, 92:8 e.r.
21, R = NHAc, 47%, 89.5:10.5 e.r.

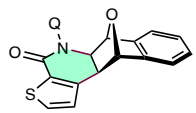

22, 67%, 93:7 e.r.

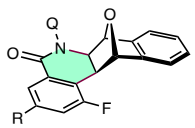

23, R = F, 80%, 83:17 e.r.
24, R = Me, 79%, 82.5:17.5 e.r.

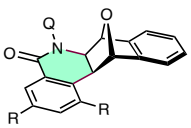

25, R = OMe, 64%, 94:6 e.r.
26, R = OAc, 33%, 90:10 e.r.

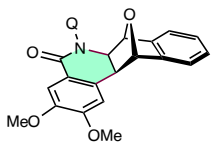

27, 72%, 92:8 e.r.

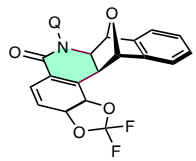

28, 85%, 88:12 e.r.

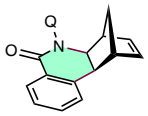

29, 34%, 83.5:16.5 e.r.[a]

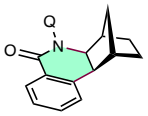

30, 37%, 89:11 e.r.[a]

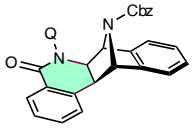

31, 50%, 96:4 e.r.

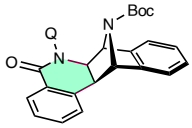

32, 45%, 96:4 e.r.

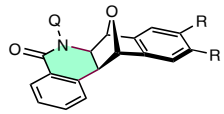

33, R = Me, 76%, 94.5:5.5 e.r.
34, R = Br, 52%, 95:5 e.r.
35, R = F, 52%, 96.5:3.5 e.r.

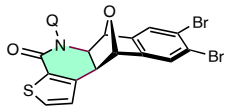

36, 50%, 95:5 e.r.

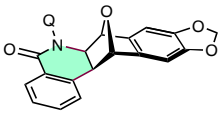

37, 68%, 94.5:5.5 e.r.

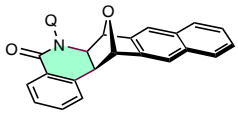

38, 65%, 91:9 e.r.

Fig. 3 | Development and scope of nickel-catalysed enantioselective electrochemical C–H activation. a, Reaction optimization: **1** (0.2 mmol), **2** (0.3 mmol), $Ni(OAc)_2·4H_2O$ (0.04 mmol), **L7** (0.04 mmol), Cp_2Fe (0.06 mmol), $BmimPF_6$ (0.05 M), 1,4-dioxane/DMA (9:1, v/v, 5 ml). Undivided cell. Ni, nickel foam cathode; stirring rate, 600 rpm. CCE at 1.5 mA. 100 °C, 15 h reaction time. During optimization carboacylation product **4** was not observed. **b**, Monitoring of the reaction progress with and without the addition of Cp_2Fe by NMR spectroscopy using 4,4′-dimethylbenzophenone as the standard. Experimental details are provided in the Supplementary Methods. **c**, Chiral and achiral ligands evaluated under the optimized reaction conditions. **d**, Versatility of nickel-catalysed enantioselective electrochemical C–H activation under optimized conditions. Isolated yields. [a]Alkene (4.0 mmol).

https://doi.org/10.1038/s41929-025-01306-9

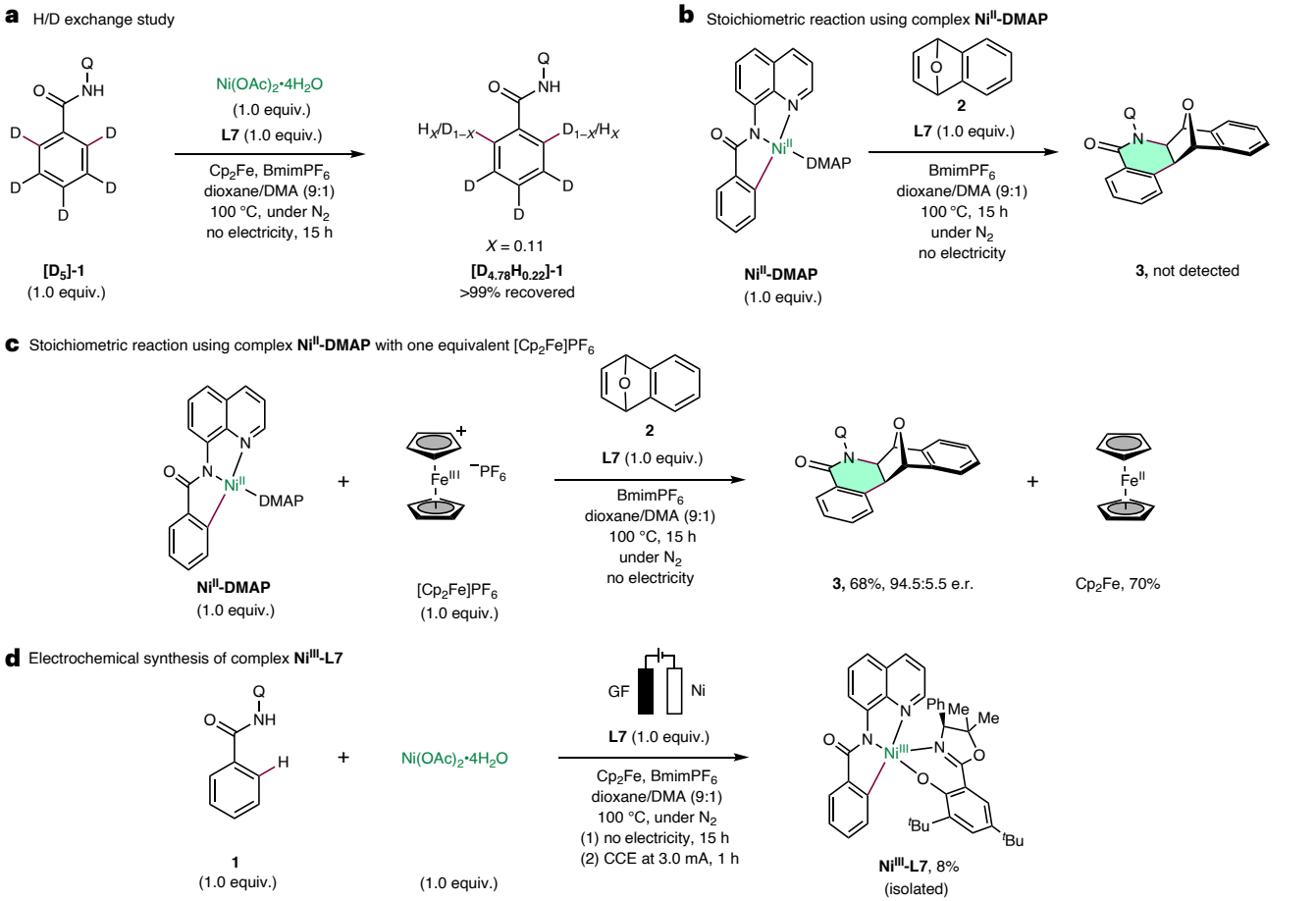

Fig. 4 | Mechanistic elucidation of the nickel-electrocatalysed C–H activation process. a, Determination of the reversibility of C–H activation through H/D exchange study. **b**, Stoichiometric reaction using complex **Ni^{II}-DMAP** with alkene **2** showing no product formation. **c**, Stoichiometric reaction using complex **Ni^{II}-DMAP** with alkene **2** with $[Cp_2Fe]PF_6$ as redox reagent leading to product **3**. **d**, Synthesis of the cyclometallated complex **Ni^{III}-L7** under electrochemical conditions. The structure of **Ni^{III}-L7** is derived from the X-ray structure obtained for complex **Ni^{III}-L11** (CCDC 2278180).

[D_5]-1, respectively), indicating a facile C–H cleavage under the catalytic conditions (for details, see 'KIE study for nickel catalysis' in the Supplementary Methods). Then, a hydrogen-deuterium (H/D) scrambling experiment was performed with substrate **[D_5]-1** and nickel(II) acetate in the absence of electricity (Fig. 4a). Here, it was discovered that C–H activation is mediated by nickel(II), as substantial H/D exchange was observed in the *ortho* positions of the recovered substrate **[$D_{4.78}H_{0.22}$]-1**. However, when the cyclometallated nickel(II) complex **Ni^{II}-DMAP** was used with alkene **2** in the presence of the chiral ligand **L7** in a stoichiometric reaction, no product formation was observed, suggesting that nickel(II) is not mediating the carboamination process (Fig. 4b). Interestingly, when this reaction was conducted with the addition of one equivalent of $[Cp_2Fe]PF_6$, the desired product **3** was obtained in high yield and very good enantioselectivity (Fig. 4c). This finding underscores the role of Cp_2Fe as a redox mediator in the electrocatalysis and suggests that the carboamination is enabled by an additional oxidation event. Therefore, the synthesis of a cyclometallated nickel(III) complex was next attempted by reacting substrate **1** with nickel(II) acetate and ligand **L7**, followed by electrolysis (Fig. 4d). This approach successfully furnished the complex **Ni^{III}-L7**, albeit in low yield.

To improve the outcome, we investigated the synthesis of **Ni^{III}-L7** starting from the cyclometallated nickel(II) complex **Ni^{II}-DMAP** (Fig. 5a). To this end, **Ni^{II}-DMAP** was subjected to a reaction with one equivalent of $[Cp_2Fe]PF_6$ and the chiral ligand **L7**. To our delight, after 15 min of reaction time, a colour change from orange to dark red was observed and the cyclometallated complex **Ni^{III}-L7** could be isolated in good yield, thereby recovering the stoichiometrically generated Cp_2Fe. To determine the relevant oxidation state of the nickel catalyst involved in the carboamination process and to confirm the importance of complex **Ni^{III}-L7** as an intermediate in the electrocatalysis, the reactivity of **Ni^{III}-L7** was investigated in a stoichiometric reaction with alkene **2** (Fig. 5b). Here, product **3** was formed in high yield and excellent enantiomeric purity, pointing to a feasible reductive elimination from nickel(III).

As the present experimental studies reveal that the nickel(II/III) redox event is crucial for the devised electrocatalysis, we further investigated the synthesized nickel complexes by cyclic voltammetry (Fig. 5c). Whereas the oxidation potential of Cp_2Fe is below the oxidation potential of **Ni^{II}-DMAP** in combination with ligand **L7** with a potential difference of less than 200 mV, the cyclometallated complex **Ni^{III}-L7** shows no oxidation event in the relevant potential range. Furthermore, a catalytic current in the cyclic voltammogram of Cp_2Fe was observed when **Ni^{II}-DMAP** together with **L7** was added, indicated by a disappearance of the reduction wave and an enhancement of the oxidation wave (for further details, see 'Electroanalytical investigations for nickel catalysis' in the Supplementary Methods). These findings further support the hypothesis of Cp_2Fe as a redox mediator via outer-sphere electron transfer[77] in the nickel(II/III) redox event. Subsequently, the nickel(II/III) interconversion was investigated by ultraviolet–visible absorption spectroelectrochemistry (UV–vis SEC) (Fig. 5d,e). To this end, the UV–vis spectra of the components were recorded, whereby a marked change was not visible in the spectrum when **Ni^{II}-DMAP** and **L7**

https://doi.org/10.1038/s41929-025-01306-9

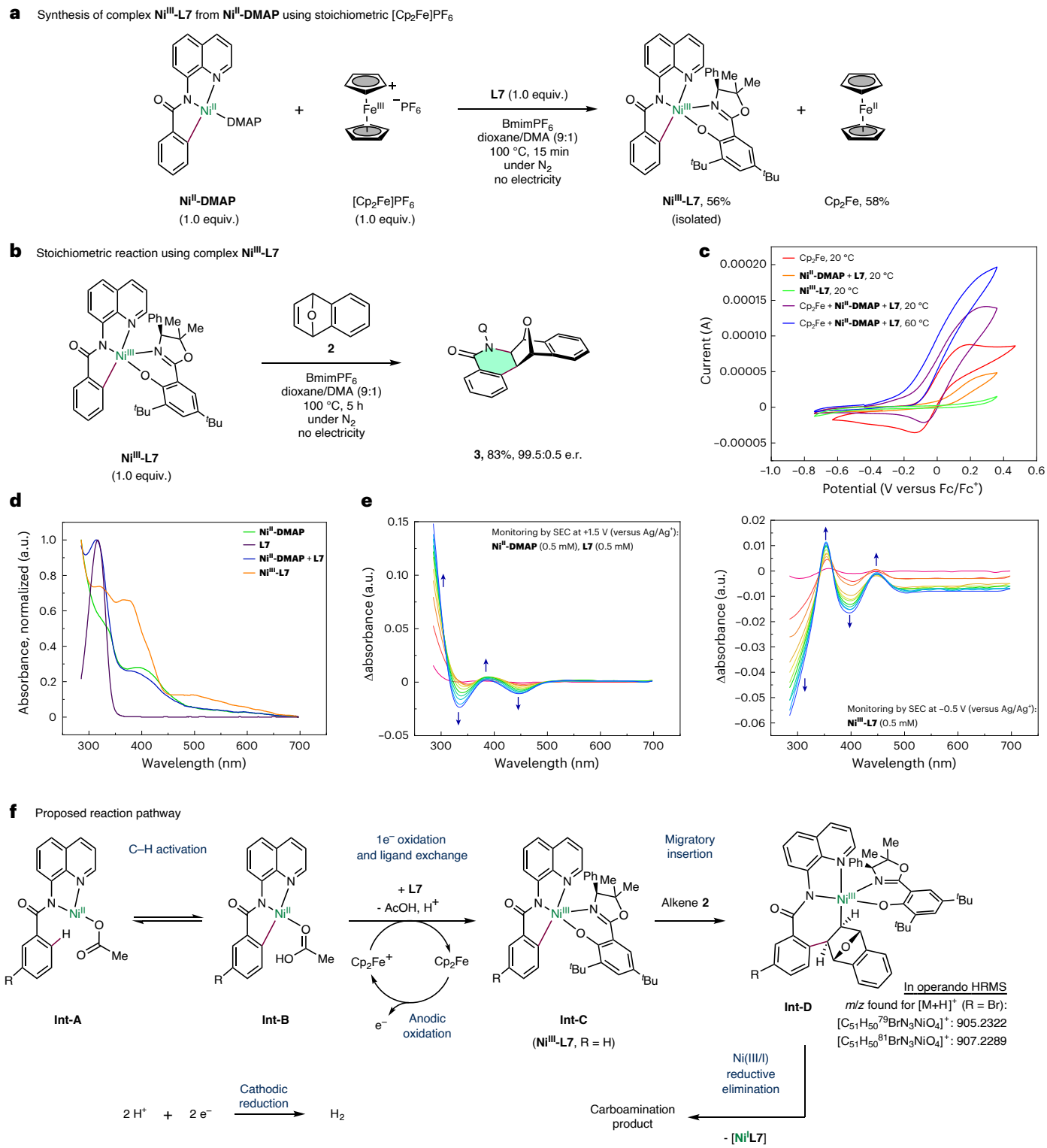

Fig. 5 | Mechanistic insights into the nickel-catalysed carboamination process. **a**, Synthesis of the cyclometallated complex **Ni^{III}-L7** with $[Cp_2Fe]PF_6$ as redox reagent. **b**, Stoichiometric reaction using complex **Ni^{III}-L7** with alkene **2**. **c**, Cyclic voltammograms to probe Cp_2Fe as the redox mediator. Cyclic voltammograms measured at 50 mV s^{-1} using dioxane/DMA (4:1) and *n*-Bu_4NPF_6 (0.1 M) as the electrolyte. **d**, UV–vis spectra of **Ni^{II}-DMAP** (0.5 mM), **L7** (0.5 mM), **Ni^{II}-DMAP** (0.5 mM) with **L7** (0.5 mM), and **Ni^{III}-L7** (0.5 mM) in dioxane/DMA (4:1) at 20 °C. **e**, SEC analysis of complex **Ni^{II}-DMAP** and **Ni^{III}-L7** with dioxane/DMA (4:1) and *n*-Bu_4NPF_6 (0.1 M) as the electrolyte. **f**, Proposed reaction pathway for nickel-catalysed carboamination. HRMS, high-resolution mass spectrometry; Fc/Fc$^+$, ferrocene/ferrocenium redox pair.

were combined, which could point to an immediate ligand exchange (Fig. 5d). In the analysis by UV–vis SEC, the change in absorbance in direct proximity to the working electrode was recorded as a function of time while applying defined potentials. Here, when +1.5 V (versus Ag/Ag$^+$) was applied in a solution of **Ni^{II}-DMAP** with **L7**, a pattern in the absorbance change was revealed, being the mirror image to the pattern observed for **Ni^{III}-L7** at −0.5 V (versus Ag/Ag$^+$) (Fig. 5e). This finding reflects the feasibility of the conversion of cyclometallated

https://doi.org/10.1038/s41929-025-01306-9

a

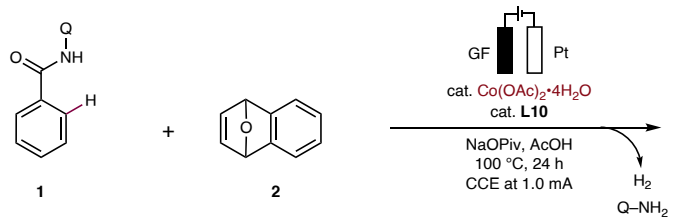

Entry	Deviation from the standard conditions	Yield **4**	e.r. **4**	d.r. **4**
1	–	75%	95:5	>20:1
2	**L6** instead of **L10**	75%	93.5:6.5	>20:1
3	**L7** instead of **L10**	50%	91:9	>20:1
4	**L8** instead of **L10**	53%	50:50	>20:1
5	**L9** instead of **L10**	78%	50:50	>20:1
6	No ligand	15%	50:50	>20:1
7	Addition of Cp_2Fe (30 mol%)	17%	93:7	>20:1
8	$Ni(OAc)_2{\cdot}4H_2O$ instead of $Co(OAc)_2{\cdot}4H_2O$	n.d.	–	–
9	No current	n.d.	–	–
10	Stoichiometric reaction using **Co^{III}-L10**, no current	30%	98:2	>20:1

b

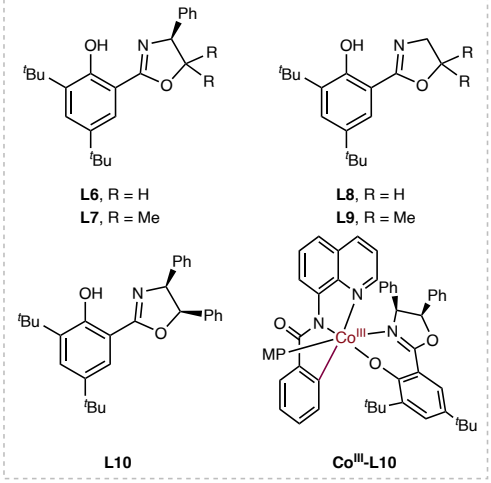

c

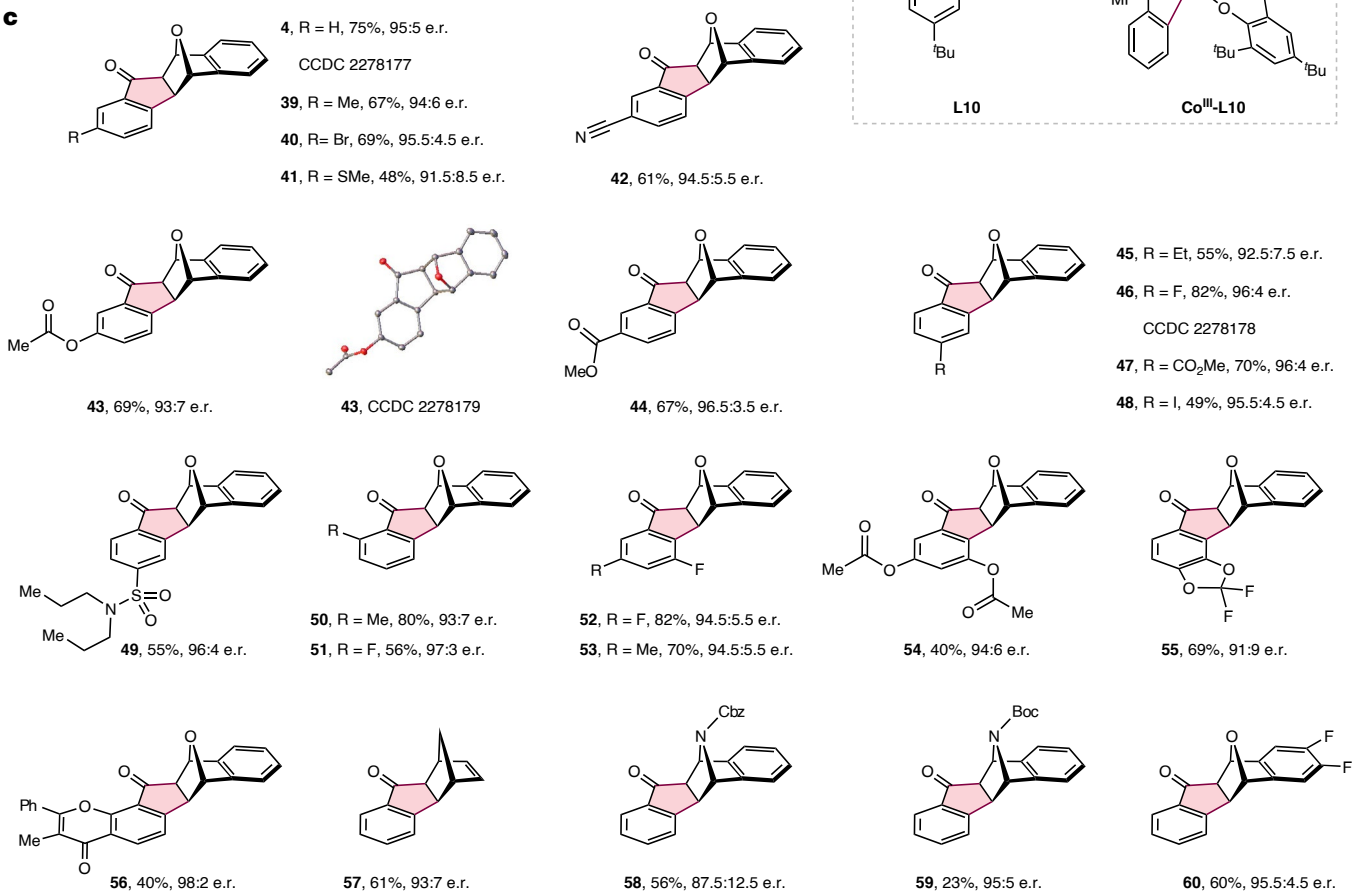

Fig. 6 | Enantioselective carboacylation by cobalt-electrocatalysed C–H activation. a, Reaction development. Reaction conditions for catalytic reactions: **1** (0.2 mmol), **2** (0.3 mmol), $Co(OAc)_2{\cdot}4H_2O$ (0.04 mmol), **L10** (0.06 mmol), NaOPiv (0.6 mmol), AcOH (5 ml). Undivided cell. Stirring rate, 600 rpm CCE at 1.0 mA; 100 °C, 24 h reaction time. During optimization carboamination, product **3** was obtained in up to 15% yield. Experimental details for stoichiometric reaction with cyclometallated complex **Co^{III}-L10** are provided in the Supplementary Methods. MP, 4-methoxypyridine. **b**, Chiral and achiral ligands investigated as well as the complex **Co^{III}-L10**. **c**, Versatility of enantioselective cobalt-catalysed C–H activation under optimized conditions. Isolated yields.

nickel(II) to nickel(III) species induced by electron transfer (for further details, see 'Electroanalytical investigations for nickel catalysis' in the Supplementary Methods). To gain further insights into the C–H/N–H activation pathway, the electrocatalytic reaction was monitored by high-resolution electrospray ionization–mass spectrometry under the standard conditions using a bromo-substituted benzamide for

https://doi.org/10.1038/s41929-025-01306-9

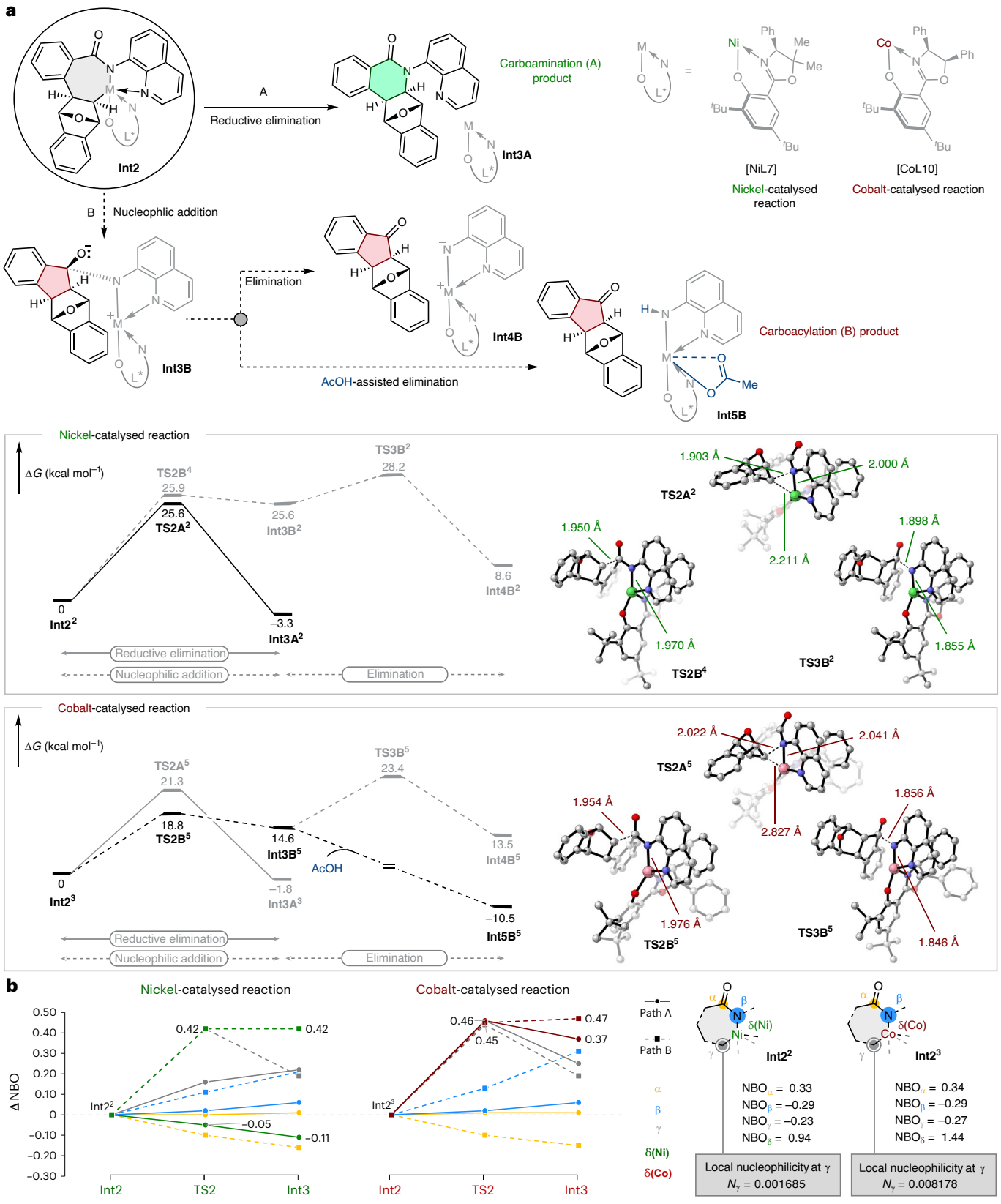

Fig. 7 | Energy profiles for product-determining step. a, Free energy diagrams of cobalt- and nickel-catalysed carboamination (A) and carboacylation (B) step. Computed relative Gibbs free energies ($\Delta G_{373.15}$) in kcal mol^{-1}. See the Supplementary Methods for complete energy profiles. Calculations were performed at the PW6B95-D4/def2-TZVPP+SMD(1,4-dioxane^{Ni}/aceticacid^{Co})// TPSS-D3(BJ)/def2-SVP level of theory. **b**, Plot for the change in NBO charges, plot for the chemodivergent step and local nucleophilicity at the γ atom. Superscripted numbers (1/3/5 and 2/4/6) in each stationary point label represent the spin multiplicity. Non-relevant hydrogens in the transition state structures were omitted for clarity.

clearly identifiable isotopic patterns. Here, a species corresponding to the nickel(III)-intermediate resulting from migratory insertion was detected by in-operando spectrometry (for details, see 'Monitoring the nickel catalysis by mass spectrometry' in the Supplementary Methods). Based on the insights gained from the mechanistic studies, a reaction pathway is proposed, as depicted in Fig. 5f. As for the cathodic half reaction, the headspace of the electrochemical cell after catalysis was analysed by gas chromatography and molecular hydrogen was detected, supporting HER as the cathodic process (see 'Detection of hydrogen gas for nickel catalysis' in the Supplementary Methods).

Cobalt electrocatalysis reveals chemoselectivity switch

To our delight, in contrast to the devised oxidative nickel electrocatalysis, which exclusively furnished carboamination product **3**, we could identify reaction conditions to favour a carboacylation pathway to furnish product **4** under cobalt electrocatalysis (Fig. 6). Conspicuously, the electrocatalytic enantioselective transformation of benzamide **1** and alkene **2** proceeded with high efficacy in the presence of the chiral ligand **L10**, giving **4** in high levels of enantio- and diastereoselectivity (Fig. 6a, entry 1, and Fig. 6b). When the achiral ligands **L8** or **L9** were used in lieu of the chiral ligand **L10**, the racemic product was formed with a diastereoselectivity of >20:1 (Fig. 6a, entries 4 and 5). Interestingly, and in contrast to the described nickel electrocatalysis, Cp_2Fe was ineffective as a redox mediator in the cobalt electrocatalysis (Fig. 6a, entry 7), which could further be confirmed by detailed cyclic voltammetry studies (see 'Electroanalytical investigations for cobalt catalysis' in the Supplementary Methods). Electricity was crucial for product formation (entry 9), whereas the electrochemically synthesized cyclometallated complex $\mathbf{Co^{III}}$**-L10** could furnish the desired product with high selectivity in a stoichiometric fashion (entry 10). The enantioselective desymmetrization strategy encompassed a broad scope (Fig. 6c), yielding the desired carboacylation products (**4** and **39**–**60**) in high yields and excellent enantiomeric control, including substrates bearing thioether (**41**), cyano (**42**) or carboxylic ester (**43**, **44**, **47** and **54**) groups, among others. Interestingly, the chemoselectivity switch was also observed for norbornadiene (**57**) and 7-azabenzonorbornadienes (**58** and **59**).

Origin of chemodivergence

Subsequently, DFT calculations were performed to rationalize the observed chemoselectivity in electrocatalysis (Fig. 7a) (for complete reaction profiles, see the Supplementary Methods and Supplementary Figs. 34 and 47). For the nickel catalysis, in line with the experimental findings, the calculations pointed to the reductive elimination as product-determining step as the most favourable pathway with an energy barrier of 25.6 kcal mol^{-1} (**TS2A²**), while for the cobalt catalysis, the nucleophilic addition resulting in carboacylation was kinetically more favourable with an energy barrier of 18.8 kcal mol^{-1} (**TS2B⁵**). Further investigation of an elimination pathway from the carboacylation intermediate **Int3B** to the final product **Int4B** also found to be unfavourable in nickel catalysis with an energy barrier of 28.2 kcal mol^{-1}. Moreover, for acetic acid (AcOH) as a solvent in cobalt catalysis, the elimination pathway with AcOH participation was considered as an alternative pathway. Inclusion of AcOH in the cobalt catalysis was crucial for the formation of the thermodynamically favoured final product **Int5B**. To gain insights into the origin of the chemoselectivity for both considered reactions, we took a closer look at the changes in the NBO charges (ΔNBO) at the key atoms α, β, γ, δ(Ni) and δ(Co) throughout the respective elementary step (Fig. 7b). Interestingly, a clear change in the charge densities magnitude could be observed for the two metals' varying behaviour. Furthermore, the local nucleophilicity[78], N_γ (see 'NBO charge analysis' in the Supplementary Methods), at γ for **Int2** in nickel and cobalt catalysis was considered, and it could be observed that the γ in cobalt catalysis is more likely (~4.8 times) to undergo nucleophilic attack than in nickel catalysis.

Conclusions

Enantioselective electro-oxidative high-valent nickel-catalysed C–H activation was achieved by data-science-guided ligand optimization. Intriguingly, by using enantioselective cobalt in lieu of nickel electrocatalysis, a switch in chemoselectivity from carboamination to carboacylation was revealed. Both devised electrocatalyses proceeded with high enantio- and diastereoselectivity providing direct access to versatile chiral building blocks with multiple stereocentres and ample scope enabled by the formation of molecular hydrogen through HER. Detailed mechanistic investigations provided valuable insights into the differences of the nickel and cobalt regime. Studies with isolated cyclometallated intermediates involving electroanalytical techniques shed light on the nickel(II/III/I) manifold. The study presented here showcases the potential of electrochemical C–H activation by 3*d* transition-metal catalysis as an innovative and powerful tool for sustainable synthesis.

Methods

General procedure for nickel catalysis

The electrolysis was carried out in an undivided cell setup. A graphite felt anode (20 mm × 10 mm × 4 mm) and a nickel foam cathode (10 mm × 15 mm × 1.4 mm) with electrode holders made of stainless steel were used. The cell was charged with the amide (0.20 mmol, 1.0 equiv), alkene (0.30 mmol, 1.5 equiv), $Ni(OAc)_2{\cdot}4H_2O$ (10 mg, 0.04 mmol), ligand **L7** (15.2 mg, 0.04 mmol), Cp_2Fe (11.2 mg, 0.06 mmol), $BmimPF_6$ (73.9 mg, 0.05 M) and a teflon-coated magnetic stirring bar (15 × 6 mm). Then, 1,4-dioxane (4.5 ml) and *N*,*N*-dimethylacetamide (DMA) (0.5 ml) were added. The reaction mixture was stirred at 100 °C for 10 min to obtain a homogeneous solution. Subsequently, the electrolysis was performed at 100 °C with a constant current of 1.5 mA maintained for 15 h with a stirring rate of 600 rpm. After completion of the reaction, the reaction mixture was diluted with 2 ml ethyl acetate and transferred to a round-bottom flask. The electrodes (nickel foam and graphite felt) were washed in the reaction flask with ethyl acetate (3 × 5 ml) in an ultrasonic cleaner (3 × 3 min), and the washes were combined in the round-bottom flask. The solvent was then removed under vacuum, and the residue was purified by column chromatography to afford the title compound.

General procedure for cobalt catalysis

The electrolysis was carried out in an undivided cell setup. A graphite felt anode (20 mm × 10 mm × 4 mm) and a platinum plate cathode (20 mm × 10 mm × 0.125 mm) with electrode holders made of stainless steel were used. The cell was charged with the benzamide (0.20 mmol, 1.0 equiv), alkene (0.30 mmol, 1.5 equiv), $Co(OAc)_2{\cdot}4H_2O$ (10 mg, 0.04 mmol), ligand **L10** (25.7 mg, 0.06 mmol), NaOPiv (0.6 mmol) and a teflon-coated magnetic stirring bar (15 × 6 mm). Then, AcOH (5.0 ml) was added. The reaction mixture was stirred at 100 °C for 10 min to obtain a homogeneous solution. Subsequently, the electrolysis was performed at 100 °C with a constant current of 1.0 mA maintained for 24 h with a stirring rate of 600 rpm. After completion of the reaction, the reaction mixture was diluted with 2 ml ethyl acetate and transferred to a round-bottom flask. The electrodes (platinum plate and graphite felt) were washed in the reaction flask with ethyl acetate (3 × 5 ml) in an ultrasonic cleaner (3 × 3 min), and the washes were combined in the round-bottom flask. The solvent was then removed under vacuum, and the residue was purified by column chromatography to afford the title compound.

Data availability

The data supporting the findings of this study are available within the Article and its Supplementary Information. The generated datasets, optimized ligand coordinates and Python code for data analysis and regression model optimization are provided as part of the Supplementary Information. Crystallographic data are available free of charge

under Cambridge Crystallographic Data Centre (CCDC) reference numbers 2278177 (**4**), 2278175 (**9**), 2278176 (**11**), 2278179 (**43**), 2278178 (**46**) and 2278180 (**Ni^{III}-L11**). All other requests for materials and information should be addressed to the corresponding author.

References

1. Siu, J. C., Fu, N. & Lin, S. Catalyzing electrosynthesis: a homogeneous electrocatalytic approach to reaction discovery. *Acc. Chem. Res.* **53**, 547–560 (2020).
2. Ghosh, M., Shinde, V. S. & Rueping, M. A review of asymmetric synthetic organic electrochemistry and electrocatalysis: concepts, applications, recent developments and future directions. *Beilstein J. Org. Chem.* **15**, 2710–2746 (2019).
3. Malapit, C. A. et al. Advances on the merger of electrochemistry and transition metal catalysis for organic synthesis. *Chem. Rev.* **122**, 3180–3218 (2022).
4. Novaes, L. F. T. et al. Electrocatalysis as an enabling technology for organic synthesis. *Chem. Soc. Rev.* **50**, 7941–8002 (2021).
5. Yan, M., Kawamata, Y. & Baran, P. S. Synthetic organic electrochemical methods since 2000: on the verge of a renaissance. *Chem. Rev.* **117**, 13230–13319 (2017).
6. Cheng, X. et al. Recent applications of homogeneous catalysis in electrochemical organic synthesis. *CCS Chem.* **4**, 1120–1152 (2022).
7. Rein, J., Zacate, S. B., Mao, K. & Lin, S. A tutorial on asymmetric electrocatalysis. *Chem. Soc. Rev.* **52**, 8106–8125 (2023).
8. Sbei, N., Hardwick, T. & Ahmed, N. Green chemistry: electrochemical organic transformations via paired electrolysis. *ACS Sustain. Chem. Eng.* **9**, 6148–6169 (2021).
9. Martínez, N. P., Isaacs, M. & Nanda, K. K. Paired electrolysis for simultaneous generation of synthetic fuels and chemicals. *New J. Chem.* **44**, 5617–5637 (2020).
10. Chen, G., Li, X. & Feng, X. Upgrading organic compounds through the coupling of electrooxidation with hydrogen evolution. *Angew. Chem. Int. Ed.* **61**, e202209014 (2022).
11. Dotan, H. et al. Decoupled hydrogen and oxygen evolution by a two-step electrochemical–chemical cycle for efficient overall water splitting. *Nat. Energy* **4**, 786–795 (2019).
12. Ball, M. & Weeda, M. The hydrogen economy—vision or reality? *Int. J. Hydrog. Energy* **40**, 7903–7919 (2015).
13. Turner, J. A. Sustainable hydrogen production. *Science* **305**, 972–974 (2004).
14. Zeng, A. et al. Battery technology and recycling alone will not save the electric mobility transition from future cobalt shortages. *Nat. Commun.* **13**, 1341 (2022).
15. Zhang, L., Chen, Z., Yang, C. & Xu, Z. Global supply risk assessment of the metals used in clean energy technologies. *J. Clean. Prod.* **331**, 129602 (2022).
16. Frey, J., Hou, X. & Ackermann, L. Atropoenantioselective palladaelectro-catalyzed anilide C–H olefinations viable with natural sunlight as sustainable power source. *Chem. Sci.* **13**, 2729–2734 (2022).
17. Dhawa, U. et al. Enantioselective palladaelectro-catalyzed C–H olefinations and allylations for N–C axial chirality. *Chem. Sci.* **12**, 14182–14188 (2021).
18. Dhawa, U. et al. Enantioselective pallada-electrocatalyzed C–H activation by transient directing groups: expedient access to helicenes. *Angew. Chem. Int. Ed.* **59**, 13451–13457 (2020).
19. Huang, Y.-Q. et al. Electrochemical rhodium-catalyzed enantioselective C–H annulation with alkynes. *CCS Chem.* **4**, 3181–3189 (2022).
20. Wei, W., Scheremetjew, A. & Ackermann, L. Electrooxidative palladium- and enantioselective rhodium-catalyzed [3 + 2] spiroannulations. *Chem. Sci.* **13**, 2783–2788 (2022).
21. Zhou, G. et al. Electrooxidative rhodium(III)/chiral carboxylic acid-catalyzed enantioselective C–H annulation of sulfoximines with alkynes. *Angew. Chem. Int. Ed.* **63**, e202319871 (2024).
22. von Münchow, T., Dana, S., Xu, Y., Yuan, B. & Ackermann, L. Enantioselective electrochemical cobalt-catalyzed aryl C–H activation reactions. *Science* **379**, 1036–1042 (2023).
23. Lin, Y., von Münchow, T. & Ackermann, L. Cobaltaelectro-catalyzed C–H annulation with allenes for atropochiral and P-stereogenic compounds: late-stage diversification and continuous flow scale-up. *ACS Catal.* **13**, 9713–9723 (2023).
24. Li, T. et al. Cobalt-catalyzed atroposelective C–H activation/annulation to access N–N axially chiral frameworks. *Nat. Commun.* **14**, 5271 (2023).
25. Yao, Q.-J., Huang, F.-R., Chen, J.-H., Zhong, M.-Y. & Shi, B.-F. Enantio- and regioselective electrooxidative cobalt-catalyzed C–H/N–H annulation with alkenes. *Angew. Chem. Int. Ed.* **62**, e202218533 (2023).
26. Zhou, G. et al. Base-promoted electrochemical Co^{II}-catalyzed enantioselective C–H oxygenation. *Angew. Chem. Int. Ed.* **62**, e202302964 (2023).
27. Liu, T. et al. Synthesis of P-stereogenic cyclicphosphinic amide via electrochemical enabled cobalt-catalyzed enantioselective C–H annulation. *Green Chem.* **25**, 3606–3614 (2023).
28. Si, X.-J. et al. Cobalt-catalyzed enantioselective C–H/N–H annulation of aryl sulfonamides with allenes or alkynes: facile access to C–N axially chiral sultams. *Chem. Sci.* **14**, 7291–7303 (2023).
29. Haynes, W. M. *CRC Handbook of Chemistry and Physics, 97th Edition* (CRC Press, 2016).
30. 32400 USD/kg (palladium), 30.9 USD/kg (cobalt), 16.2 USD/kg (nickel). *MineralPrices* (Mineral Fund Advisory, accessed 14 December 2023) https://mineralprices.com/ (2023).
31. Nuss, P. & Eckelman, M. J. Life cycle assessment of metals: a scientific synthesis. *PLoS ONE* **9**, e101298 (2014).
32. *ICH Guideline Q3D (R2) on Elemental Impurities* 5–14 (European Medicines Agency, 2020).
33. Chernyshev, V. M. & Ananikov, V. P. Nickel and palladium catalysis: stronger demand than ever. *ACS Catal.* **12**, 1180–1200 (2022).
34. Tasker, S. Z., Standley, E. A. & Jamison, T. F. Recent advances in homogeneous nickel catalysis. *Nature* **509**, 299–309 (2014).
35. Zhu, C., Chen, H., Yue, H. & Rueping, M. Electrochemical chemo- and regioselective arylalkylation, dialkylation and hydro(deutero) alkylation of 1,3-enynes. *Nat. Synth.* **2**, 1068–1081 (2023).
36. Ruan, L.-X., Sun, B., Liu, J.-M. & Shi, S.-L. Dynamic kinetic asymmetric arylation and alkenylation of ketones. *Science* **379**, 662–670 (2023).
37. Cao, Y.-X., Wodrich, M. D. & Cramer, N. Nickel-catalyzed direct stereoselective α-allylation of ketones with non-conjugated dienes. *Nat. Commun.* **14**, 7640 (2023).
38. Shu, X., Zhong, D., Huang, Q., Huan, L. & Huo, H. Site- and enantioselective cross-coupling of saturated N-heterocycles with carboxylic acids by cooperative Ni/photoredox catalysis. *Nat. Commun.* **14**, 125 (2023).
39. Liang, K., Zhang, Q. & Guo, C. Nickel-catalyzed switchable asymmetric electrochemical functionalization of alkenes. *Sci. Adv.* **8**, eadd7134 (2022).
40. Liang, K., Zhang, Q. & Guo, C. Enantioselective nickel-catalysed electrochemical cross-dehydrogenative amination. *Nat. Synth.* **2**, 1184–1193 (2023).
41. Hu, X., Cheng-Sánchez, I., Cuesta-Galisteo, S. & Nevado, C. Nickel-catalyzed enantioselective electrochemical reductive cross-coupling of aryl aziridines with alkenyl bromides. *J. Am. Chem. Soc.* **145**, 6270–6279 (2023).

42. Liu, D. et al. Paired electrolysis-enabled nickel-catalyzed enantioselective reductive cross-coupling between α-chloroesters and aryl bromides. *Nat. Commun.* **13**, 7318 (2022).
43. Qiu, H. et al. Enantioselective Ni-catalyzed electrochemical synthesis of biaryl atropisomers. *J. Am. Chem. Soc.* **142**, 9872–9878 (2020).
44. DeLano, T. J. & Reisman, S. E. Enantioselective electroreductive coupling of alkenyl and benzyl halides via nickel catalysis. *ACS Catal.* **9**, 6751–6754 (2019).
45. Wang, Y.-Z. et al. Nickel/biimidazole-catalyzed electrochemical enantioselective reductive cross-coupling of aryl aziridines with aryl iodides. *Nat. Commun.* **14**, 2322 (2023).
46. Chatani, N. Nickel-catalyzed functionalization reactions involving C–H bond activation via an amidate-promoted strategy and its extension to the activation of C–F, C–O, C–S, and C–CN bonds. *Acc. Chem. Res.* **56**, 3053–3064 (2023).
47. Liu, Y.-H., Xia, Y.-N. & Shi, B.-F. Ni-catalyzed chelation-assisted direct functionalization of inert C–H bonds. *Chin. J. Chem.* **38**, 635–662 (2020).
48. Diesel, J., Finogenova, A. M. & Cramer, N. Nickel-catalyzed enantioselective pyridone C–H functionalizations enabled by a bulky N-heterocyclic carbene ligand. *J. Am. Chem. Soc.* **140**, 4489–4493 (2018).
49. Wang, Y.-X. et al. Enantioselective Ni–Al bimetallic catalyzed exo-selective C–H cyclization of imidazoles with alkenes. *J. Am. Chem. Soc.* **140**, 5360–5364 (2018).
50. Wang, Y.-X. et al. Enantioselective nickel-catalyzed C(sp^3)–H activation of formamides. *Angew. Chem. Int. Ed.* **61**, e202209625 (2022).
51. Woźniak, Ł. & Cramer, N. Enantioselective C–H bond functionalizations by 3*d* transition-metal catalysts. *Trends Chem.* **1**, 471–484 (2019).
52. Loup, J., Dhawa, U., Pesciaioli, F., Wencel-Delord, J. & Ackermann, L. Enantioselective C–H activation with earth-abundant 3*d* transition metals. *Angew. Chem. Int. Ed.* **58**, 12803–12818 (2019).
53. Zahra, R. et al. A review on nickel cobalt sulphide and their hybrids: earth abundant, pH stable electro-catalyst for hydrogen evolution reaction. *Int. J. Hydrog. Energy* **45**, 24518–24543 (2020).
54. Flett, D. S. Cobalt–nickel separation in hydrometallurgy: a review. *Chem. Sustain. Dev.* **12**, 81–91 (2004).
55. Slater, J. C. Atomic radii in crystals. *J. Chem. Phys.* **41**, 3199–3204 (1964).
56. Allred, A. L. Electronegativity values from thermochemical data. *J. Inorg. Nucl. Chem.* **17**, 215–221 (1961).
57. Danopoulos, A. A., Simler, T. & Braunstein, P. N-heterocyclic carbene complexes of copper, nickel, and cobalt. *Chem. Rev.* **119**, 3730–3961 (2019).
58. Barefield, E. K., Busch, D. & Nelson, S. Iron, cobalt, and nickel complexes having anomalous magnetic moments. *Q. Rev. Chem. Soc.* **22**, 457–498 (1968).
59. Klein, H.-F. Trimethylphosphane complexes of nickel, cobalt, and iron—model compounds for homogeneous catalysis. *Angew. Chem. Int. Ed.* **19**, 362–375 (1980).
60. Liu, X. et al. Aspergichromones A–E, five chromone derivatives with complicated polycyclic architecture from *Aspergillus deflectus*. *Org. Lett.* **24**, 1610–1615 (2022).
61. Liu, D.-L. et al. Acerinol, a cyclolanstane triterpenoid from *Cimicifuga acerina*, reverses ABCB1-mediated multidrug resistance in HepG2/ADM and MCF-7/ADR cells. *Eur. J. Pharmacol.* **733**, 34–44 (2014).
62. Tse, E. G. et al. Nonclassical phenyl bioisosteres as effective replacements in a series of novel open-source antimalarials. *J. Med. Chem.* **63**, 11585–11601 (2020).
63. Calvo-Martín, G. et al. Norbornene and related structures as scaffolds in the search for new cancer treatments. *Pharmaceuticals* **15**, 1465 (2022).
64. Subbaiah, M. A. M. & Meanwell, N. A. Bioisosteres of the phenyl ring: recent strategic applications in lead optimization and drug design. *J. Med. Chem.* **64**, 14046–14128 (2021).
65. Skhiri, A. & Chatani, N. Nickel-catalyzed reaction of benzamides with bicylic alkenes: cleavage of C–H and C–N bonds. *Org. Lett.* **21**, 1774–1778 (2019).
66. Gandeepan, P., Rajamalli, P. & Cheng, C.-H. Diastereoselective [3+2] annulation of aromatic/vinylic amides with bicyclic alkenes through cobalt-catalyzed C–H activation and intramolecular nucleophilic addition. *Angew. Chem. Int. Ed.* **55**, 4308–4311 (2016).
67. Vivek Kumar, S., Yen, A., Lautens, M. & Guiry, P. J. Catalytic asymmetric transformations of oxa- and azabicyclic alkenes. *Chem. Soc. Rev.* **50**, 3013–3093 (2021).
68. Bolm, C., Weickhardt, K., Zehnder, M. & Ranff, T. Synthesis of optically active bis(2-oxazolines): crystal structure of a 1,2-bis(2-oxazolinyl)benzene $ZnCl_2$ complex. *Chem. Ber.* **124**, 1173–1180 (1991).
69. Keith, J. A. et al. Combining machine learning and computational chemistry for predictive insights into chemical systems. *Chem. Rev.* **121**, 9816–9872 (2021).
70. Oliveira, J. C. A. et al. When machine learning meets molecular synthesis. *Trends Chem.* **4**, 863–885 (2022).
71. Durand, D. J. & Fey, N. Computational ligand descriptors for catalyst design. *Chem. Rev.* **119**, 6561–6594 (2019).
72. Harper, K. C., Bess, E. N. & Sigman, M. S. Multidimensional steric parameters in the analysis of asymmetric catalytic reactions. *Nat. Chem.* **4**, 366–374 (2012).
73. Milo, A., Bess, E. N. & Sigman, M. S. Interrogating selectivity in catalysis using molecular vibrations. *Nature* **507**, 210–214 (2014).
74. Niemeyer, Z. L., Milo, A., Hickey, D. P. & Sigman, M. S. Parameterization of phosphine ligands reveals mechanistic pathways and predicts reaction outcomes. *Nat. Chem.* **8**, 610–617 (2016).
75. Orlandi, M., Coelho, J. A. S., Hilton, M. J., Toste, F. D. & Sigman, M. S. Parametrization of non-covalent interactions for transition state interrogation applied to asymmetric catalysis. *J. Am. Chem. Soc.* **139**, 6803–6806 (2017).
76. Bursch, M. et al. Understanding and quantifying London dispersion effects in organometallic complexes. *Acc. Chem. Res.* **52**, 258–266 (2019).
77. Francke, R. & Little, R. D. Redox catalysis in organic electrosynthesis: basic principles and recent developments. *Chem. Soc. Rev.* **43**, 2492–2521 (2014).
78. Soleymani, M. Theoretical study on the [4+2] cycloaddition of 1,3-dimethylindole with 2,6-dimethylquinone. *Struct. Chem.* **30**, 1173–1184 (2019).

Acknowledgements

We gratefully acknowledge support from the ERC Advanced Grant no. 101021358, the DFG (Gottfried Wilhelm Leibniz award and SPP 2363 to L.A.) and the FCI (Kekulé-Fellowship no. 110091 to T.v.M. and no. 114311 to S.E.P.). We thank C. Golz (University of Göttingen) for the assistance with the X-ray diffraction analysis and J. C. A. Oliveira (University of Göttingen) for the helpful discussions and comments on the manuscript.

Author contributions

L.A. supervised the project. L.A. and T.v.M. conceived the work. T.v.M. designed the experimental studies. N.K.P. designed and conducted the computational studies. T.v.M., S.D., P.B., S.E.P., J.B., Y.-R.L. and A.S. conducted the experiments. T.v.M. and S.E.P. conducted the experimental mechanistic studies. L.A., T.v.M. and N.K.P. wrote the paper. L.A., T.v.M., N.K.P. and S.D. edited the paper.

Funding
Open access funding provided by Georg-August-Universität Göttingen.

Competing interests
The authors declare no competing interests.

Additional information
Supplementary information The online version contains supplementary material available at https://doi.org/10.1038/s41929-025-01306-9.

Correspondence and requests for materials should be addressed to Lutz Ackermann.

Peer review information *Nature Catalysis* thanks Chen Zhu and the other, anonymous, reviewer(s) for their contribution to the peer review of this work.